Fundamental measure theory for the electric double layer: implications for blue-energy harvesting and water desalination

2015 J. Phys.: Condens. Matter 27 194129

(http://iopscience.iop.org/0953-8984/27/19/194129)

IOP Publishing Journal of Physics: Condensed Matter
J. Phys.: Condens. Matter **27** (2015) 194129 (12pp) doi:10.1088/0953-8984/27/19/194129

Fundamental measure theory for the electric double layer: implications for blue-energy harvesting and water desalination

Andreas Härtel, Mathijs Janssen, Sela Samin and René van Roij

Institute for Theoretical Physics, Center for Extreme Matter and Emergent Phenomena, Utrecht University, Leuvenlaan 4, 3584 CE Utrecht, The Netherlands

E-mail: Andreas.Hartel@anno1982.de and R.vanRoij@uu.nl

Received 18 September 2014, revised 17 December 2014
Accepted for publication 8 January 2015
Published 29 April 2015

Abstract

Capacitive mixing (CAPMIX) and capacitive deionization (CDI) are promising candidates for harvesting clean, renewable energy and for the energy efficient production of potable water, respectively. Both CAPMIX and CDI involve water-immersed porous carbon (supercapacitors) electrodes at voltages of the order of hundreds of millivolts, such that counter-ionic packing is important for the electric double layer (EDL) which forms near the surfaces of these porous materials. Thus, we propose a density functional theory (DFT) to model the EDL, where the White-Bear mark II fundamental measure theory functional is combined with a mean-field Coulombic and a mean spherical approximation-type correction to describe the interplay between dense packing and electrostatics, in good agreement with molecular dynamics simulations. We discuss the concentration-dependent potential rise due to changes in the chemical potential in capacitors in the context of an over-ideal theoretical description and its impact on energy harvesting and water desalination. Compared to less elaborate mean-field models our DFT calculations reveal a higher work output for blue-energy cycles and a higher energy demand for desalination cycles.

Keywords: capacitive mixing, blue energy, desalination, density funcional theory, supercapacitors, restricted primitive model, electric double layer

(Some figures may appear in colour only in the online journal)

1. Introduction

Two of the most stringent challenges mankind faces in the coming century are the ever-growing worldwide demands for energy and fresh water. The shortages in these resources cannot be seen separately since the generation of fresh water with current techniques is an energy consuming process. However, either energy or fresh water often is available regionally. Thus, apart from alternative sources like offshore ground water [1] or solar and wind power, it is of interest to consider low-cost processes which generate energy 'using' fresh water and the other way round.

It has been known for a long time that the irreversible mixing of two distinct fluids is a spontaneous process which rises the entropy and dissipates free energy. In the case of mixing fresh and salty water that occurs when rivers flow into the sea, this Gibbs free energy of mixing amounts to (the order of) 2 kJ per liter of river water, the equivalent of a 200 m waterfall [2]. Considering the worldwide amount of water flowing into the sea, the harvest of this energy could account for a few percent of the global energy needs. Furthermore, the reverse process de-mixes salt water into brine and fresh water and requires at least the same amount of energy as its corresponding blue-energy process harvests.

The Gibbs free energy of mixing is harvested in so-called blue engines which often rely on membranes to selectively intercept some of the involved particles [3], either cations, anions, or water. Test factories have been built, based either on water-permeable membranes in the case of pressure retarded osmosis [4, 5] or ion-selective membranes in the case of reverse electro dialysis [6]. The downside of all these techniques however is that membranes are costly and tend

to foul upon exposure to the large amounts of water flowing through them.

A promising alternative to the techniques mentioned above has recently been offered by Brogioli [7]. He proposed the use of porous carbon electrodes to selectively mix the liquids in a four-stroke charging-desalination-discharging-resalination cycle, very much in the spirit of a Stirling heat engine that performs an expansion-cooling-compression-reheating cycle. Within this capacitive mixing (CAPMIX) process [8], the charging of the electrodes takes place while immersed in salty water, whereas they are discharged in fresh water. The de- and resalination steps are performed by flushing the electrodes with fresh and sea water, respectively, which enlarges or compresses the electric double layer (EDL). Such cycles have a net positive work output, because the expansion/compression of the EDL changes the capacitance and thereby the potential (at fixed charge on the electrode). More specifically, salty water more effectively screens the charge on the electrode surfaces such that charging steps are performed at lower potential than discharging steps. In the reverse process of capacitive desalination (CDI) energy is consumed to lower the salinity of a finite volume (say a bucket) of water, while salt ions are released into the sea or a reservoir (the performance of this process has been studied in [9]).

Interestingly, all devices discussed have a broader applicability than just the mixing of sea- and river water since they do not put severe restrictions on the type of solutions that are mixed. For instance, energy can also be harvested from mixing CO_2 with air [10], because CO_2 produces charged carbonic acids when it is flushed through water. These acid particles can subsequently play the same role in a CAPMIX process as the salt ions in water in a conventional blue engine cycle.

In contrast to membranes, porous carbons couple a huge internal surface area of the order of a square km per kg to long lifetimes and low manufacturing costs [11, 12]. For this reason, they can for instance also be used in ionic liquid-filled (super)capacitors to store large amounts of energy. In fact, due to the safety of ionic liquids and high (dis)charging rates, supercapacitors are already used in buses and planes. The porous-material properties are highly determined by the distribution of pore-sizes [13], where the physics inside a pore depends on its shape [14, 15] and size [16–18]. Thus, tuning the porous structure of the material [19] helps to optimize the storage of energy within supercapacitors. These findings motivate us to investigate whether similar phenomena can be observed in the aqueous electrolyte-filled supercapacitors of blue engines and desalination devices. As a starting point we focus on a quasi-static description leaving dynamic effects associated with optimal power [20] for later studies.

The (macroscopic) behaviour of the materials and devices discussed above is determined by the EDL which forms in the (microscopic) region close to the electrodes' surface. A lot of research has been performed on its theoretical modeling, dating back to Gouy–Chapman's analytical solution of the Poisson–Boltzmann equation for point-like ions in contact with a charged planar wall [21, 22]. However, this simple theory fails to capture the rich variety of phenomena as observed in more advanced models that do take into account the steric repulsion between ions in the EDL, e.g. simulation studies [23–25], phenomenological extensions [26, 27], or bottom-up density functional approaches [28–37], leading to phenomena like a bell-shape capacitance at high salt concentrations [26], oscillations in capacitance [24] and an anomalous capacitance increase in sub-nanometer pores [25]. In the case of (classical) density functional theory [38], the hard-sphere repulsion is included from first principles. Beyond the restricted primitive model of equally charged hard spheres in contact with a charged hard wall, further physics has been addressed, for example by a more realistic treatment of water [39], the polarization of particles [40], or the asymmetry of ions [41–43].

In this work, we study blue-energy and desalination devices within the restricted primitive model using a modern density functional theory (DFT) approach. To construct our functional, we follow the work of Mier-y-Teran *et al* [30], including pure Coulombic and hard-sphere correlations as well as residual correlations from the mean spherical approximation (MSA). Thereby, we avoid the use of an arbitrary weight function that enters in the recently proposed weighted correlation approach FMT/WCA-k^2 [35], which has been used in a study of the electric double layer in slit-like pores [44]. In contrast to previous work [18, 30, 33, 35, 37, 40, 44–47], we describe the pure hard-sphere interactions using the White Bear mark II approach [48] within fundamental measure theory [49, 50]. To our knowledge, this approach describes hard spheres within DFT most accurately and even predicts the crystalline phase and its coexistence with the fluid phase quantitatively [51, 52]. Our research focusses on the fundamental understanding of the cyclic CAPMIX and CDI processes, in particular on the molecular structure of the densely-packed electrolyte confined in the pores of the charged nanoporous electrode. Finally, we discuss optimal cycle characteristics, taking previous thermodynamical consideration into account [53, 54].

2. Set-up

A so-called *blue engine* consists of a supercapacitor which can be connected to sea and river reservoirs and performs a sequence of charging and discharging steps to harvest *blue energy*. A *desalination device* also consists of a supercapacitor, but it is connected to a finite-sized bucket which is desalinated and subsequently refilled (after securing the fresh water) with salty water from a sea reservoir in a cyclic fashion.

In our work, the supercapacitor consists of two porous carbon electrodes at potentials Ψ_+ and Ψ_- as sketched in figure 1. Here, a typical porous electrode consists of a broad distribution of pore sizes which are classified as macropores (>50 nm), mesopores (2–50 nm) and micropores (<2 nm) [55]. The macropores act as transport channels and are globally charge neutral, whereas the micropores have most impact on the storage of charges, in particular due to overlapping double layers. We model the electrode to consist solely of equally sized pores, where we choose either micropores of a typical size $L = 2$ nm within such electrodes or mesopores of $L = 8$ nm, a width were packing constraints are less severe.

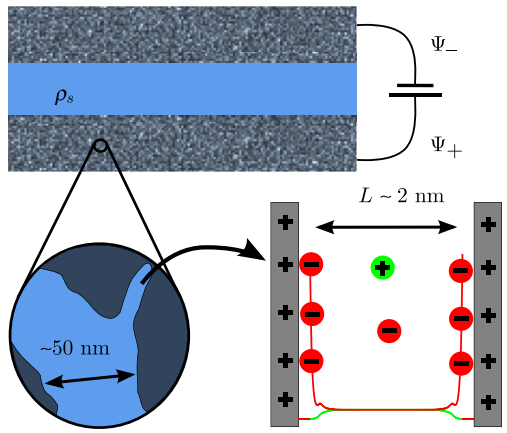

Figure 1. Sketch of the supercapacitor as used in blue engines and desalination devices. Two porous carbon electrodes are set to the potentials Ψ_+ and Ψ_- and are immersed in a monovalent ion solution with salt concentration ρ_s. The porous material contains pores of several sizes. The small pores are modeled as parallel plate capacitors of plate separation or pore size L.

The pores in one electrode have a total volume $V_{\mathrm{el}} = L \times A$ and are described by a parallel plate capacitor of plate area A and separation L; we call L the pore size. The capacitor plates are located at $z = 0$ and $z = L$ and are kept at the same potential as the macroscopic electrode they belong to. Accordingly, they carry like-charge densities $e\sigma$, resulting in a total electrode charge $Q = 2Ae\sigma$, where we introduced the elementary unit charge e. Furthermore, we neglect size effects of the parallel plate capacitor by taking the limit $A \to \infty$ such that the system is described solely by one spatial coordinate z, perpendicular to the plates. For symmetry reasons we only need to model the macroscopic anode of our blue engine with a pore volume V_{el} and a pore size L. The cathode is just an oppositely charged mirror image of the anode.

To describe the ions in water we apply the restricted primitive model, where a binary mixture of oppositely charged hard spheres is confined between two planar charged hard walls. Accordingly, the cations and anions are modeled by monodisperse charged hard spheres of radius $R = R_+ = R_- = 0.34\,\mathrm{nm}$ (as used in [53, 56]) that carry the charges Z_+e and Z_-e, respectively and already contain the surrounding hydration shell of polarized solvent molecules for each ion. In this work, the ions of interest are Na^+ and Cl^- ions of valencies $Z_+ = 1$ and $Z_- = -1$. As in previous work [57, 58], the remaining homogeneous dielectric solvent is characterized by a relative dielectric constant $\varepsilon = 78.54$ at a temperature $T = 298.15\,\mathrm{K}$. For this setting, the Bjerrum length $\lambda_{\mathrm{B}} = e^2/(4\pi\varepsilon_0\varepsilon k_{\mathrm{B}}T)$ with the vacuum permittivity ε_0 and the Boltzmann constant k_{B} amounts to $\lambda_{\mathrm{B}} = 0.714\,\mathrm{nm}$. The resulting Debye screening length κ^{-1} with $\kappa^2 = 4\pi\lambda_{\mathrm{B}}(Z_+^2 + Z_-^2)\rho_s$, ranges from $\kappa^{-1} = 0.43\,\mathrm{nm}$ to $\kappa^{-1} = 2.15\,\mathrm{nm}$ for bulk salt concentrations between $\rho_s = 0.5\,\mathrm{M}$ (sea water) and $\rho_s = 0.02\,\mathrm{M}$ (river water), respectively. Now, the particle interaction between two ions i and j at a distance r reads

$$\Phi_{ij}(r) = \begin{cases} \infty & r < 2R; \\ k_{\mathrm{B}}T\lambda_{\mathrm{B}}\dfrac{Z_iZ_j}{r} & r \geqslant 2R. \end{cases} \tag{1}$$

Similarly, the steric interaction between the pore walls and a cation or anion at position z is

$$V_\pm^{\mathrm{ext}}(z) = k_{\mathrm{B}}T \begin{cases} \infty & (z < R_\pm) \text{ or } (L - z < R_\pm); \\ 0 & \text{otherwise.} \end{cases} \tag{2}$$

Here, the steric repulsion between the hydrated ions and the wall naturally leads to a so-called Stern layer of the same thickness as the hydrated-ion radius R. Within this Stern layer, the concentration of charged particles remains zero, while we assume no change of the dielectric constant to avoid additional polarization effects.

Now, we define the overall unit-charge density as

$$q\big(z; [\rho_+, \rho_-, \sigma]\big) = Z_+\rho_+(z) + Z_-\rho_-(z) + \sigma\delta(z) + \sigma\delta(z - L), \tag{3}$$

containing contributions from cations and anions via their one-particle number densities $\rho_\pm$ and from the surface charge density $e\sigma$ localized on the electrodes at $z = 0$ and $z = L$.

3. Theory

We use density functional theory (DFT) [38, 59] to describe the system of densely-packed ions and charged walls within each of the macroscopic electrodes. Within this theoretical framework, the grand potential $\Omega(T, V, \mu_+, \mu_-, \Psi)$ of the equilibrated system can be written as a functional $\Omega(T, V, \mu_+, \mu_-, \Psi; [\rho_+, \rho_-, \sigma])$ of the one-particle number densities $\rho_\pm$ of the cations and anions and of the wall unit-charge density σ for a temperature T, a volume V, ionic chemical potentials $\mu_\pm$ and an electrostatic wall-potential $\Psi = \Psi_+ = -\Psi_-$. The grand potential naturally follows from the intrinsic Helmholtz free energy $F(T, V, N_+, N_-, Q)$ via a generalized Legendre transform

$$\begin{aligned} &\Omega\big(T, V, \mu_+, \mu_-, \Psi; [\rho_+, \rho_-, \sigma]\big) \\ &\quad = F\big(T, V; [\rho_+, \rho_-, \sigma]\big) \\ &\qquad -2e\Psi A\sigma + \sum_{i=\pm} A\int_0^L \Big(V_i^{\mathrm{ext}}(z) - \mu_i\Big)\rho_i(z)\mathrm{d}z, \end{aligned} \tag{4}$$

where the number density profiles $\rho_\pm$ and the unit-charge density profile σ represent the extensive particle numbers $N_\pm = A\int_0^L \rho_\pm(z)\mathrm{d}z$ and electrode charge $Q = 2eA\sigma$. In the presence of particle interactions the intrinsic free energy $F = F_{\mathrm{id}} + F_{\mathrm{exc}}$ is usually split into an ideal gas part F_{id} (see e.g. [60]) and an excess part F_{exc} that contains the (remaining) interactions. Minimized by the equilibrium density and charge profiles, the functional finally yields the Euler–Lagrange equations

$$\mu_\pm = V_\pm^{\mathrm{ext}}(z) + \left.\frac{\delta F\big(T, V; [\rho_+, \rho_-, \sigma]\big)}{\delta\rho_\pm(z)}\right|_{\rho_\pm = \rho_\pm^{\mathrm{eq}}}, \tag{5}$$

$$\Psi = (2eA)^{-1}\left.\frac{\delta F_{\mathrm{exc}}\big(T, V; [\rho_+, \rho_-, \sigma]\big)}{\delta\sigma}\right|_{\sigma = \sigma^{\mathrm{eq}}}. \tag{6}$$

As in previous work [30, 46], the excess free energy functional $F_{\mathrm{exc}} = F_{\mathrm{C}} + F_{\mathrm{HS}} + F_{\mathrm{corr}}$ in our restricted primitive

model contains the excess terms F_C and F_{HS} due to the pure Coulomb and hard-sphere interactions, as well as an excess term F_{corr} which gives rise to residual correlations. Here, the excess correlation term F_{corr} follows from the analytically known solution of the Ornstein–Zernike equation in the mean spherical approximation (MSA) closure in the bulk [61]. Furthermore, the mean-field Coulomb term F_C typically defines the (dimensionless) electrostatic potential $\phi(z) = \frac{e}{k_B T}\psi(z)$ via the formal solution of the Poisson equation. This electrostatic potential connects to the electrostatic wall potential Ψ via $\Psi = \psi(0) = \psi(L)$ and allows to extract the unit-charge density σ using Gauss' law. New in our description, the hard-sphere interactions are modeled within fundamental measure theory (FMT) via the White-Bear mark II functional [48] in its tensor version [51]. This functional successfully predicts not only the freezing transition and correct free energies in a hard-sphere system [48, 51], but also the interfacial tension of a crystal-fluid interface [52]. Henceforth, we call this density functional approach *FMT-PB-MSA*, referring to the three contributions to the excess free energy. For comparisons, we also introduce *FMT-PB*, where we set the excess term $F_{corr} = 0$.

In the limit $R \to 0$ of charged point-like ions, the excess part F_{HS} of the free energy that describes the short-ranged hard-sphere interactions vanishes. Accordingly, the excess correlation term F_{corr} also disappears. To preserve the Stern layer in this limit, we do not apply $R \to 0$ to the external potential $V_\pm^{ext}$ in equation (2) for this *PB+S* approach, but replace the particle radius R with the thickness R_S of the Stern layer. We furthermore consider the case without Stern layer by setting $R_S = 0$, henceforth referred to as *PB*. For comparison, we also consider the so-called modified Poisson–Boltzmann theory (*mPB*) [26], where steric ion effects are included using a lattice-gas ansatz.

3.1. Simulation methods

To test our theoretical results, we perform molecular dynamics simulations (*Sim*) of spherical particles with diameters $2R$ and charges $\pm e$ using the ESPResSo package [62, 63]. For the short-range part of the pair interaction we use the pseudo hard-sphere potential

$$u_{ij} = \begin{cases} \frac{50^{50}}{49^{49}}\epsilon\left[\left(\frac{2R}{r_{ij}}\right)^{50} - \left(\frac{2R}{r_{ij}}\right)^{49}\right] + \epsilon, & r_{ij} < \frac{50}{49}2R \\ 0, & r_{ij} \geqslant \frac{50}{49}2R \end{cases} \quad (7)$$

where r_{ij} is the distance between two particles i and j and ϵ is the interaction parameter. This cut-and-shifted generalized Lennard-Jones potential is suitable for use in continuous molecular dynamics simulations and was found to reproduce structural and thermodynamical data of hard-spheres accurately over the whole fluid range [64]. The particles are confined between two charged hard walls of distance L, whereby the short range interaction with the walls is also given by equation (7). The long-ranged Coulomb forces were evaluated using the P^{3}M method [65] with metallic boundary conditions. The unwanted interaction between periodically replicated slabs is subtracted using the electrostatic layer correction method [65].

In order to compare with our FMT-PB-MSA results, we perform simulations in the canonical ensemble using the ion number densities obtained from the DFT calculations, which also sets the charge density on the pore walls. Thereby, the number of particles in the pore varies between 3000–6000. We find that for large enough pores, the mid-plane bulk ion densities $\rho_\pm(L/2)$ in all the simulations agree with the FMT-PB-MSA result to within 0.5%. This indicates that our canonical simulation results agree with the grand-canonical FMT-PB-MSA calculations. The simulations are initialized from random particle configurations and are equilibrated with a Langevin thermostat at a temperature $k_B T/\epsilon = 1$. We use a time step of $\Delta t = 0.001$–0.004 (in standard simulation units), where smaller values are required for larger number densities. After an equilibration of the system for at least 2×10^5 time steps, the system was sampled every 200–800 time steps for at least 10^6 time steps. The obtained cation- and anion-density profiles are used for the calculation of the electrostatic potential profile from

$$\phi(z) = -2\pi\lambda_B \int_0^z \left[\int_0^{z'} q(z'')\mathrm{d}z'' - \int_{z'}^L q(z'')\mathrm{d}z''\right]\mathrm{d}z', \quad (8)$$

where $q(z)$ is defined in equation (3). This relation yields the potential in slit systems with Neumann boundary conditions up to an arbitrary constant [66]. We choose this constant such that the midplane potential $\phi(L/2)$ is identical to that obtained from FMT-PB-MSA.

4. Concentration profiles

To obtain equilibrium concentration profiles $\rho_\pm(z)$, we solve the Euler–Lagrange equations (5) and (6) on a grid using a Picard iteration scheme [67]. Assuming a homogeneous concentration in directions along the pore walls, we resolve the pore width L in z-direction perpendicular to the walls with a grid spacing of $L/2000 \leqslant 0.004\,\mathrm{nm}$. With this choice the typical length scale of the system (screening length κ^{-1} or hard sphere diameter $2R$) is resolved with more than 100 grid points. We explore electrode potentials over the whole electrochemical window of water, where the limit of $2\Psi = 1.2\,\mathrm{V}$ represents the starting point of electrochemical reactions between the electrode and the solvent particles.

In figure 2, we show the resulting potential and concentration profiles for the various theories introduced in the previous section in comparison with our molecular dynamics simulations. In figures 2(*a*) and (*b*), we show potential profiles which are normalized to unity at the wall for two pores of sizes $L = 2\,\mathrm{nm}$ and $L = 8\,\mathrm{nm}$. The corresponding concentration profiles are shown in figures 2(*c*)–(*j*), where we focus on the region close to the wall. Note that the profiles within a pore are mirror symmetric with respect to the pore center.

Figure 2(*a*) shows three potential profiles from FMT-PB-MSA theory at different electrode potentials Ψ. Next to the wall, all of them have a linear part due to an ion-free Stern layer which FMT-type theories naturally predict. At high potentials, even a second Stern layer can be observed, indicating a second region free of charges in between the first and second layer

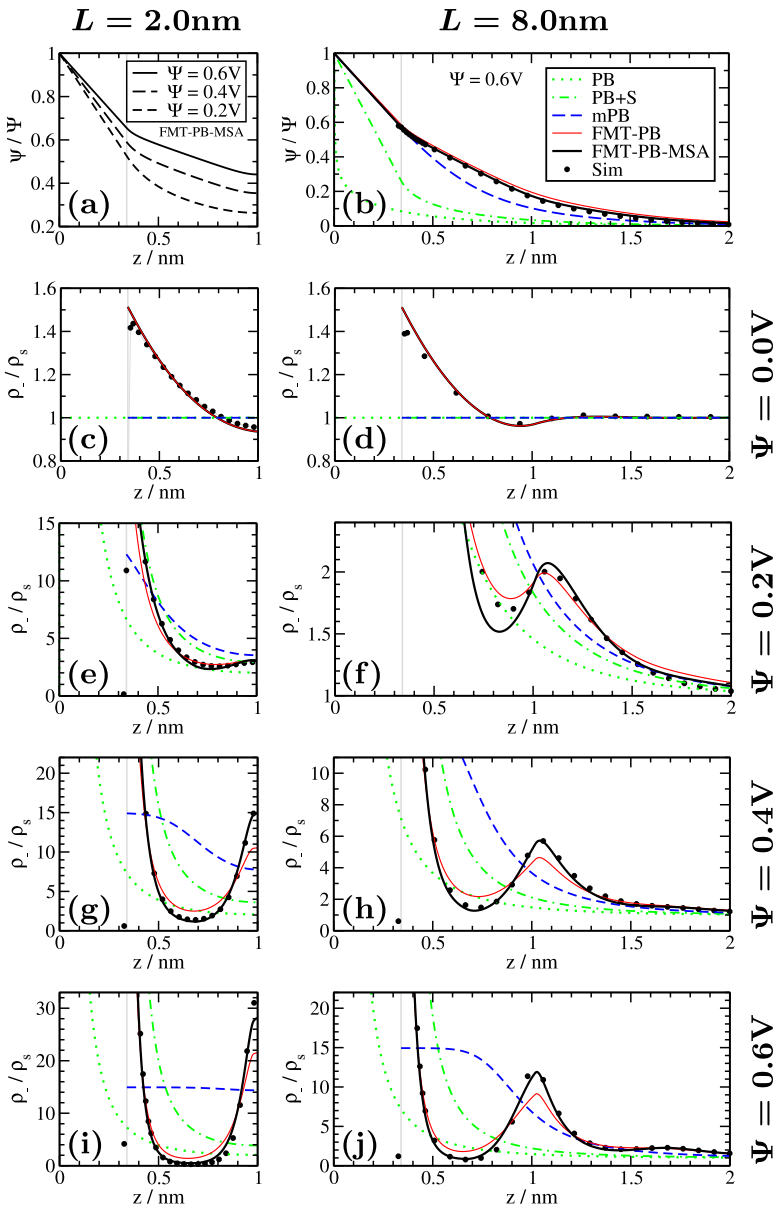

Figure 2. (*a*), (*b*) Potential profiles $\psi(z)$ and (*c*)–(*j*) counterion concentration profiles $\rho_-(z)$ at an electrode potential Ψ and a bulk concentration $\rho_s = 0.5\,\mathrm{M}$. We show data for two different pore sizes of (left column) $L = 2\,\mathrm{nm}$ and (right column) $L = 8\,\mathrm{nm}$ as well as for four electrode potentials Ψ of (*c*), (*d*) 0.0 V, (*e*), (*f*) 0.2 V, (*g*), (*h*) 0.4 V and (*i*), (*j*) 0.6 V. The potential profiles in (*a*) are solely obtained from FMT-PB-MSA theory, where all the remaining plots show data obtained from all theories investigated and our molecular dynamics simulations.

of densely packed counterions next to the wall. Such layering effects have been observed e.g. in [24, 68] and they are clearly visible in figure 2(*i*). Thus, high enough potentials repel the coions completely and lead to an increasing midplane potential $\psi(L/2)$ for increasing electrode potentials Ψ. For larger pores this effect diminishes, which can be observed in figure 2(*b*) for the mesopore of size $L = 8\,\mathrm{nm}$, where the center of the pore behaves similar to the bulk. Therefore, the mesopores play a smaller role in the salt uptake, because an excess number of ions is only contained in the electric double layer.

In figures 2(*c*) and (*d*), we start our analysis of the concentration profiles with a vanishing external potential $\Psi = 0$. In this case the pore walls are uncharged and only the FMT-type theories show inhomogeneous concentration profiles due to built-in steric interactions. Since the ions are monodisperse, both co- and counterions have the same concentration profiles and, counterintuitively, lead to a negative net salt adsorption due to the naturally predicted ion-free Stern layer. This effect has already been observed for pure hard-sphere systems [69]. For the non-vanishing potentials, PB-type models cannot capture these packing effects since they are based on an ideal gas description. Especially mPB theory underestimates the concentrations close to the electrodes and, even more, predicts a plateau for higher packings [36] as shown in figures 2(*g*), (*i*) and (*j*). Here, the almost flat concentration profile in figure 2(*i*) signifies an almost completely filled pore.

Finally, our computer simulations show excellent agreement with FMT-PB-MSA theory. As mentioned earlier, we feed the canonical simulations with particle numbers within the slit pore obtained by using a cubic spline integration

from our FMT-type theory results. Here, the simulations always recover the FMT-predicted bulk. Although the particle numbers obtained from FMT-PB and FMT-PB-MSA theory differ only slightly, corresponding simulations always fit the FMT-PB-MSA results better (not shown). Therefore, we choose the particle numbers predicted from FMT-PB-MSA theory as an input for our simulations. Figure 2 illustrates that FMT-PB-MSA theory excellently covers the details of the concentration profiles $\rho_\pm$ obtained by the simulations. Only in regions of high inhomogeneity, small deviations can be observed, e.g. in figure 2(i) in the midplane. Interestingly, figure 2(f) shows larger deviations between theory and simulations for the region around $z = 0.9\,\mathrm{nm}$ than can be observed at higher potentials. However, it is remarkable that even at high potentials and in strong confinements FMT-PB-MSA is in very good agreement with simulations.

5. Charging and capacitance

In the previous section we analyzed the potential and ion-concentration profiles for two pore widths of our model supercapacitor at a set of electrode potentials. Since we are interested in the capacitive performance of our model supercapacitor, we now study the relation between the surface charge density $e\sigma$ and the potential Ψ on the electrode. This relation is naturally related to the differential capacitance per unit surface area

$$C_{\mathrm{diff}} = \frac{\partial e\sigma}{\partial \Psi}. \tag{9}$$

In figures 3(a) and (b) we plot the relation between the electrode potential and the electrode charge density at fixed bulk salt concentrations $\rho_s = 0.5\,\mathrm{M}$ and $\rho_s = 0.02\,\mathrm{M}$, which correspond to sea and fresh river water, respectively. Since the electrode charge is limited by the maximum number of ions in a pore, the limit of close-packing in a slit-pore [70] sets the maximum electrode charge. Therefore, the surface charge density of a 2 nm pore can not exceed the maximum of approximately $3.9\,\mathrm{e\,nm^{-2}}$. An example for such a densely packed system can be seen in figure 2(i). The corresponding charge-potential curve in figure 3(a) is bound by this maximum charge density and indeed seems to converge towards it within the plotted region. In contrast, the PB and PB+S theories do not predict such a limiting charge, because they assume point-like ions. Thus, the electrode charge becomes unphysically high when potentials increase. A further comparison between figures 3(a) and (b) shows that the electrode potential at a fixed electrode charge is higher at smaller pore size within all mentioned theories.

In the next section we will discuss cyclic (dis)charging processes that follow the charge-potential strokes at low and high salt concentrations. We will see that the amount of energy, which a blue engine can harvest from a concentration gradient, is related to the voltage rise between these strokes. This rise is shown in figure 3(c) and converges towards a plateau for every choice of theory, provided that the dielectric constant is kept fixed. Since at low potentials the packing effects are not particularly pronounced, PB-type theories perform reasonably well in this regime. Deviations between the theories only start

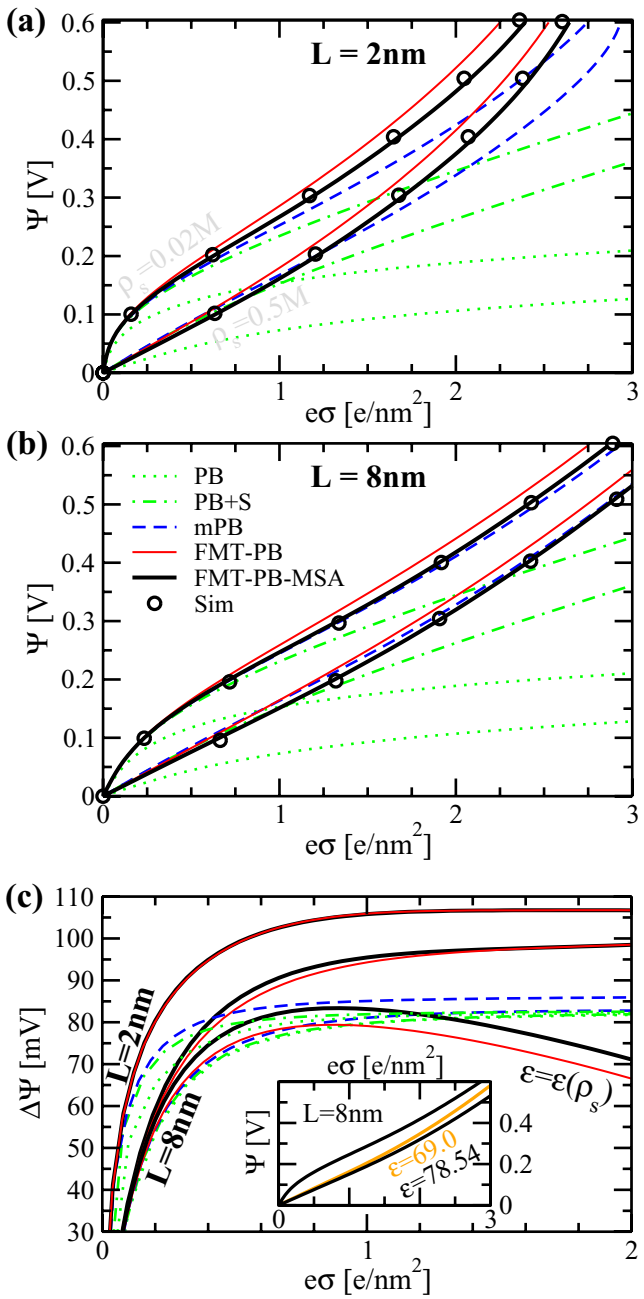

Figure 3. The charge-potential relations at two concentrations $\rho_s = 0.02\,\mathrm{M}$ and $\rho_s = 0.5\,\mathrm{M}$ shown for two pore sizes (a) $L = 2\,\mathrm{nm}$ and (b) $L = 8\,\mathrm{nm}$. The potential rise $\Delta\Psi := \Psi_{c=0.02\,\mathrm{M}} - \Psi_{c=0.5\,\mathrm{M}}$ between both *strokes* is shown in (c). In addition, we add data for the FMT-PB-MSA theory where we use a concentration-dependent ε (see text) which depends on the bulk concentration ρ_s and is constant along each grand canonical stroke.

to appear at higher potentials. In general, the maximum value of the plateau seems to be related to the charge density $e\sigma$ at which the plateau is reached. Here, the more elaborate FMT-type theories reach the plateau at higher surface charges than the less elaborate ones. However, within all these theories the mentioned plateau is reached at higher charge densities $e\sigma$ when the pore size is increased. As a result, we find that the FMT-type theories reach the highest value for $\Delta\Psi$, followed by mPB and finally PB(+S) theory with the lowest value.

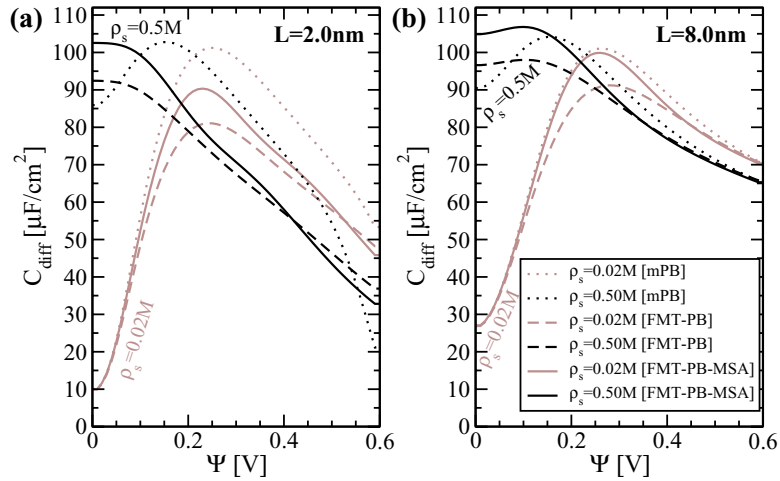

Figure 4. Differential capacitances at two bulk concentrations $\rho_s = 0.02\,\mathrm{M}$ and $\rho_s = 0.5\,\mathrm{M}$ for two pore sizes (*a*) $L = 2\,\mathrm{nm}$ and (*b*) $L = 8\,\mathrm{nm}$.

The largest possible electrostatic potential rise is limited by the chemical potential difference between the involved solutes at low and high concentration. This can be seen from the limit where coions are fully excluded from the pore and counterions are most densely packed. In contact with a reservoir at either low or high concentration, the number of coions always stays the same and the chemical potential of the reservoir sets an offset for the electrostatic potential. For PB theory this limiting difference is well-known at $\Delta\Psi \approx 83\,\mathrm{mV}$ for the salt concentrations used here, but it shifts, when other contributions than ideal gas are considered. For the additional steric contributions from the hard-sphere interactions in our FMT-type theories, the limit is higher at $\Delta\Psi \approx 107\,\mathrm{mV}$. Thus, the aforementioned corresponding waterfall [2] would be higher by a factor $107/83 \approx 1.29$.

Until now, we used a fixed dielectric constant of $\varepsilon = 78.54$. However, measurements show that the bulk dielectric constant depends on temperature and concentration [71, 72]. Keeping the temperature fixed at $T = 298.15\,\mathrm{K}$, this dependency reads $\varepsilon(\rho_s) = 78.461 - 20.0154\rho_s/M + 4.0415(\rho_s/M)^2 - 0.54052(\rho_s/M)^3$, spanning a range from $\varepsilon(0.02\mathrm{M}) = 78.06$ to $\varepsilon(0.5\mathrm{M}) = 69.4$. Taking this into account, the grand canonical charge-potential strokes change towards higher potentials (see inset of figure 3(*c*)) and the potential rise $\Delta\Psi$ reaches a maximum at a finite charge density, decreasing again for higher charges. This behaviour is shown in figure 3(*c*) within the FMT-PB-MSA theory.

The highly non-linear relation between charge and potential on the electrode is well captured by the differential capacitance as defined in equation (9). It is known that in the limiting case of infinite electrode separation within PB theory C_{diff} increases with the electrode potential as $\sim \cosh(\phi/2)$, since there is no limiting maximal charge [21, 22]. For the PB+S theory, the differential capacitance reaches a plateau at high voltage, corresponding to the capacitance of the Stern layer. Within mPB theory at infinite plate separation, the differential capacitance was found analytically [26]. Contrary to the exponential increase of Gouy–Chapman, this solution decreases with the square root of the potential for large potentials. For low concentrations it has a local minimum at $\Psi = 0\,\mathrm{V}$, which turns into a global maximum at higher packing fractions. This transition from the so-called bell to camel shape occurs when the packing parameter within mPB theory becomes $\gamma = \frac{1}{3}$ and both camel and bell shape have been found experimentally [73, 74]. Obviously, in the confining geometry of our model supercapacitor, both mPB and FMT-type theories reproduce decaying tails of C_{diff} for increasing electrode potentials, as shown in figure 4. Interestingly, at high salt concentration the FMT-type theories already passed to a bell shape in the micropores in figure 4(*a*), whereas mPB theory still predicts a camel shape. This finding can also be seen from figure 3(*a*), where the stroke corresponding to mPB theory at high concentration shows a convex curvature at low potential instead of a concave one when compared to the FMT-type results, which helps to reach the plateau in figure 3(*c*) at a small charge density $e\sigma$. Moreover, figure 2 shows that within small pores the concentration profiles in the midplane are already affected at an electrode potential $\Psi = 0\,\mathrm{V}$, which could explain the bell shape in our FMT-type results.

6. Cyclic processes

Our model supercapacitor can be charged (discharged) by connecting it to (using it as) an external power source. Thereby, the electric double layer is built up at (removed from) the porous electrodes of the system, storing (releasing) energy. If (dis)charging happens sufficiently slowly, the dynamical processes can be assumed to be quasi-static. Thereby, the (dis)charging time should be substantially larger than the RC-time, such that the system always has enough time to equilibrate and therefore stays in equilibrium. Even though real systems typically work on shorter time scales out of equilibrium we investigate the universal quasi-static behaviour as a starting point. If, now, the electrodes are in contact with a reservoir at fixed chemical potential while they are (dis)charged, the (dis)charging process is described by the grand canonical (dis)charging strokes which are shown in figure 3.

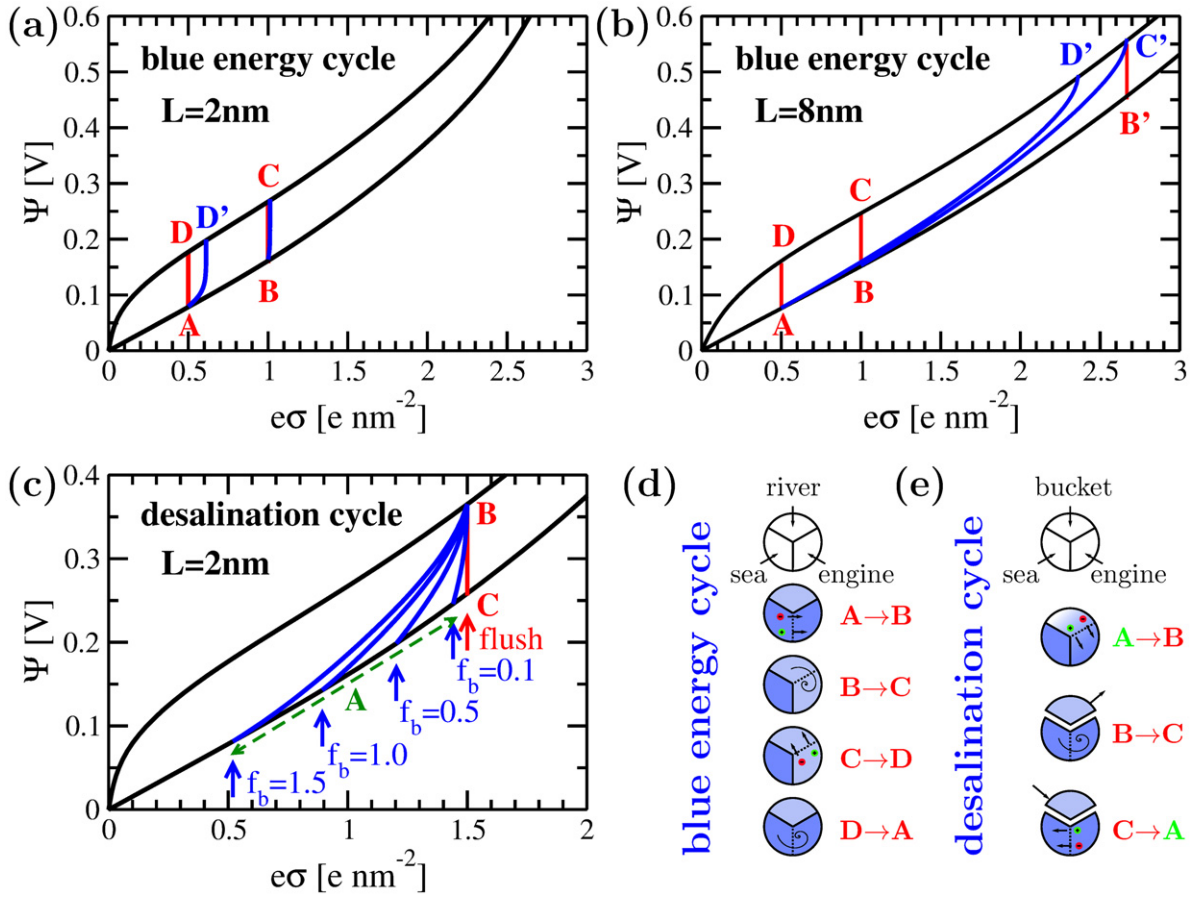

Figure 5. Blue-energy and desalination cycles in between charge-potential strokes at two concentrations $\rho_s = 0.02\,\mathrm{M}$ and $\rho_s = 0.5\,\mathrm{M}$ for two pore sizes $L = 2\,\mathrm{nm}$ (left-hand side) and $L = 8\,\mathrm{nm}$ (right-hand side). More details about the cycles are given in the text and in the process diagrams in (*d*) and (*e*).

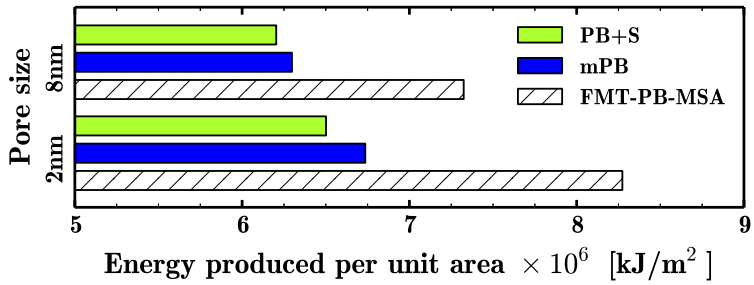

Figure 6. Energy harvested per unit surface area of the electrode material during one blue-energy cycle ABCDA as shown in figures 5(*a*) and (*b*). We compare PB+S, mPB and FMT-PB-MSA theory for both pore size $L = 2\,\mathrm{nm}$ and $L = 8\,\mathrm{nm}$.

In the previous section, we have seen that these (dis)charging strokes depend on the salt concentration within the reservoir, to which the electrodes are connected. To exploit this dependency, Brogioli recently proposed a four-stroke charging-desalination-discharging-resalination cycle to harvest a net amount of energy [7]. This process extracts the free energy which is released during the selective mixing of water at two different concentrations. Such blue-energy cycles ABCDA are shown in figures 5(*a*) and (*b*) and are explained schematically in figure 5(*d*). The cycle starts with a grand canonical charging step AB, while the engine is connected to a reservoir at high ion concentration. This step is followed by a flushing step, where the water at high ion concentration is replaced by water at low ion concentration, which rises the electrode potential while the charge on the electrode remains the same. Now, a grand canonical discharging step follows and, finally, the engine is brought back to the initial state by flushing with sea water. In fact, the total work

$$W = -\oint \Psi \mathrm{d}Q \tag{10}$$

delivered in such a cycle is positive, because the charging steps in sea water take place at a lower potential than the discharging steps in river water. In figure 6 we present the corresponding energy harvested during such blue-energy cycles ABCDA for the two pores of size $L = 2\,\mathrm{nm}$ and $L = 8\,\mathrm{nm}$ within three

of our theories. In agreement with figure 3 we find that the energy per unit surface area of the electrode is larger for smaller pores. Furthermore, it is obvious from figures 5(*a*) and (*b*) that the area enclosed by the cycle ABCDA increases with the potential rise $\Delta\Psi$ between the strokes at low and high concentration. This quantity, previously discussed and depicted in figure 3(*c*), was shown to be largest for the elaborate FMT-type theories, which is also depicted in figure 6. Since this enhanced work output is a model-dependent finding, it does not correspond to a higher work output in an experimental setting, only to a more accurate description of the physics at hand. For example, along with figure 3(*c*) we also discussed the consequences of using a dielectric constant that depends on the concentration, which results in an overall lower work output than a corresponding cycle with a fixed dielectric constant would have. Nevertheless, the mutual deviation between the theories shows that packing effects are important in the context of cyclic processes such as discussed in this work and should be taken into account.

In order to accomplish an actual increase in the work output, we distinguish two possibilities. First, the electrostatic potential not only depends on the chemical potential, but also on a set of variables like temperature, valence, or pore size. In principle, they can be tuned to make the potential rise between the two involved concentrations and the corresponding work output as large as possible. For instance, a threefold increase of the work output is possible, when instead of sea and river water at equal temperature, high-temperature (e.g. waste-heated) river water is used during the resalination step [56]. This effect has also been observed experimentally [75]. Furthermore, varying water temperature can also enhance the work output in a membrane-based setup [76].

Second, the energy dissipated during operation can be made as small as possible by choosing an optimal sequence of ensembles for the (dis)charging steps. Similar to Carnot's optimization of the Stirling cycle, the blue-energy cycle can be optimized with respect to the harvested energy per ion [53]. By mapping the intensive and extensive thermodynamic variables of the blue engine to those of a heat engine system, which operates on a thermal instead of a concentration gradient, it was shown that the Brogioli cycle is the CAPMIX analogue of a Stirling cycle [54]. Accordingly, an optimal blue engine would have a rectangular path in μN-representation of chemical potential μ and ion number N, that is, two grand-canonical steps at fixed μ and two (new) canonical steps (BC' and D'A) at fixed N. Then, each ion transported between the two reservoirs is able to donate its full $\Delta\mu$ to the harvested energy without spoiling energy in the irreversible flushing steps (BC and DA).

The order of the canonical and grand-canonical strokes is fixed by the thermodynamic relation $C_\mu > C_N$ between the differential capacitances at fixed chemical potential μ or particle number N, respectively [54]. Furthermore, from figures 5(*a*) and (*b*) it becomes obvious that the slope of the canonical strokes in the $\Psi\sigma$-representation highly depends on packing properties and, accordingly, changes when varying, for example, the particle density or the pore size. Thereby, a steep slope hints at a situation close to a limiting charge on the electrode due to close packing of ions in the pore, as discussed in the previous sections. Accordingly, the canonical strokes in figures 5(*a*) and (*b*) become steeper in the narrow micropore of $L = 2\,\mathrm{nm}$ than they are in the mesopore of $L = 8\,\mathrm{nm}$ where the center of the pore still can act as a reservoir for counterions. For very dense packings, the canonical strokes become almost vertical in the $\Psi\sigma$-representation, as we show in figure 5(*a*) where the point C' is not shown since it is almost at the same position ($\sigma = 1.01\,\mathrm{nm}^{-2}$) as the point C ($\sigma = 1.00\,\mathrm{nm}^{-2}$).

As is obvious from figure 5(*b*), the Carnot-like 'optimal' (with respect to the harvested energy per ion) cycle ABC'D'A has a smaller area than the cycle AB'C'DA. Both cycles are performed in the same potential range and for a pore volume of $V_\mathrm{e} = 2V_\mathrm{el} = 1\,\mathrm{L}$ within both electrodes, the work output of the engine is $W \approx 1.3\,\mathrm{kJ}$ and $W \approx 8.4\,\mathrm{kJ}$, respectively. Thus, a discrepancy exists between an optimal cycle in the sense of total harvested energy per cycle and harvested energy per ion. Which of the two options is more desirable depends on the availability of the required resources, in particular that of fresh water.

In addition, a well-chosen combination of canonical and grand canonical strokes is able to tune the number of ions that is passed through the engine during operation. For example, the energy output for the cycles ABC'D'A and AB'C'DA in figure 5(*a*) for an engine volume of 1 L is $W \approx 6.8\,\mathrm{kJ}$ and $W \approx 8.3\,\mathrm{kJ}$, respectively. Interestingly, the energy output of the cycle AB'C'DA seems to be similar for both pore sizes we have analyzed. This also holds for the PB+S and mPB theory (not shown), where the energy harvested during this cycle is $W \approx 7.8\,\mathrm{kJ}$ and $W \approx 7.2\,\mathrm{kJ}$ (PB+S) and $W \approx 7.5\,\mathrm{kJ}$ and $W \approx 7.3\,\mathrm{kJ}$ (mPB) for the two pores of $L = 2\,\mathrm{nm}$ and $L = 8\,\mathrm{nm}$.

Similar to its heat engine counterpart, the blue engine can also be run in reverse for desalinating water. An example of the corresponding three-stroke cycle ABCA is shown in figure 5(*c*) and explained schematically in figure 5(*e*). Starting in an initial state A, we connect the capacitor of pore volume V_e to a bucket of volume V_b which is to be desalinated. The capacitor is charged canonically, capturing the ions into the capacitor pores and desalinating the bucket. After reaching the low concentration in point B, we disconnect the bucket to harvest the fresh water and flush the capacitor with water at high ion concentration to point C. We then simultaneously refill the bucket with seawater and discharge the capacitor in contact with the sea reservoir until the initial charging state A is reached. Here the bucket and capacitor are reconnected so that the cycle can start again.

Keeping point B fixed, the location of point A in figure 5(*c*) depends on the chosen fraction $f_\mathrm{b} = V_\mathrm{b}/V_\mathrm{e}$ between the bucket and engine volumes, because the size of the connected bucket also sets the number of ions that must be adsorbed into the capacitor. For this reason, the slope of the canonical strokes AB depends on the fraction f_b. Note that this quantity is varied here by changing the bucket size, keeping the pore width and volume fixed.

Unlike a blue-energy cycle, the work in equation (10) picks up an extra minus sign in a desalination cycle because the latter runs clockwise instead of anti-clockwise in its charge-potential representation. Consequently, desalination costs energy.

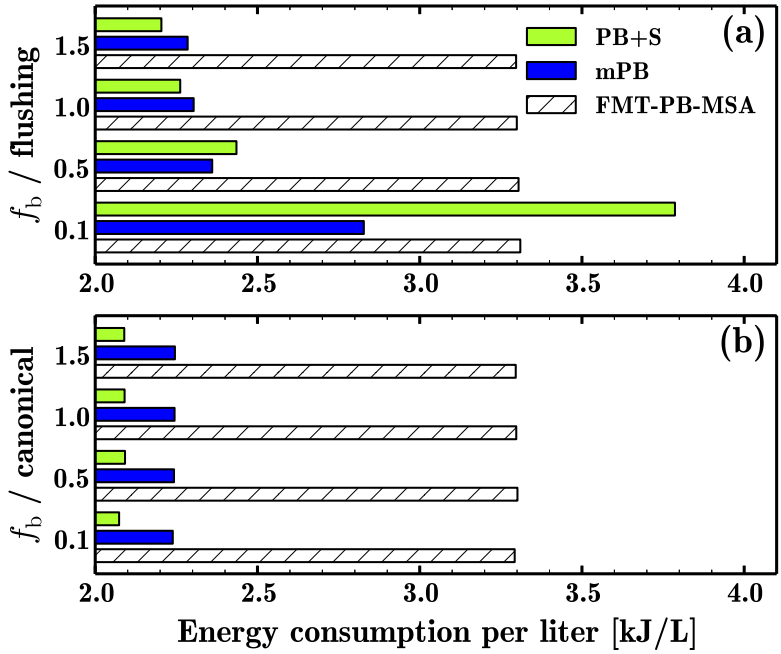

Figure 7. Energy consumption per liter of desalinated water for desalination cycles as shown in figure 5(*c*), where point B lays at $\sigma = 1.5\,\mathrm{nm}^{-2}$. We compare PB+S, mPB and FMT-PB-MSA theory for four ratios $f_b = V_b/V_e$ between bucket and engine volumes for (*a*) a flushing step BC and (*b*) a canonical step BC', respectively.

Similar to the previously discussed blue-energy cycle, to minimize energy losses the dissipative flushing step BC can be replaced by a reversible canonical step BC'. Though we will discuss these cycles in the following, we do not show point C' in figure 5(*c*) because it would almost coincide with C. Note that for larger pore sizes the points C and C' would separate more, as shown in figures 5(*a*) and (*b*) for a blue-energy cycle. The interior of larger pores namely acts more like a reservoir, such that it requires a more significant ion-release from the EDL to resalinate a larger pore. In figure 7 we compare the energy consumption during desalination cycles as shown in figure 5(*c*), for different bucket fractions f_b within PB+S, mPB and FMT-PB-MSA theory for a flushing step BC and a canonical step BC', respectively.

For the flushing-type desalination cycle, we find that FMT-type calculations predict the largest amount of consumed energy in most cases when compared to PB+S and mPB theory. This was to be expected on the basis of figure 3(*c*) which shows that potential steps with respect to different concentrations are largest in FMT-type theories. Furthermore, in figure 7(*a*) PB+S and mPB theory predict an increasing amount of required energy to desalinate one liter of water for decreasing fractions f_b and, accordingly, bucket volumes V_b, while FMT-PB-MSA theory predicts quite constant values of invested energy. This can be understood by analyzing the cycle ABCA in the limit of vanishing bucket volume V_b and fraction $f_b \to 0$. In this case of vanishing bucket size, the point A reaches the point C' and the desalination step becomes equivalent to a canonical step without desalination bucket. In other words, the work of the cycle ABCA becomes equivalent to the work that corresponds to the enclosed area C'BCC', which remains finite. For this reason, the energy per volume of desalinated water diverges in this limit. However, in FMT-type theories the enclosed area C'BCC' is much smaller than in PB+S and mPB theory due to the previously discussed packing effects and, therefore, the invested work seems to stay unaffected from the bucket size within the explored range [0.1, 1.5] of fraction f_b. Nevertheless, it will diverge if f_b becomes small enough.

If the flushing step BC is replaced by a canonical step BC', the enclosed area C'BCC' reduces to a single line which does not enclose any area. Therefore, the work per cycle vanishes for vanishing bucket volume V_b and, for this reason, no divergences should appear, as indeed observed in figure 7(*b*). Moreover, the desalination energy per liter water is constant for all fractions f_b within all mentioned theories, because the corresponding cycles are optimal with respect to the energy per ion. Accordingly, the energy per liter of desalinated water is constant.

For larger pores of $L = 8\,\mathrm{nm}$, during a desalination stroke, the total capacitor potential would almost reach the limit of 1.2 V, where electrochemical processes would start. The meso- (and macropores) therefore lower the pore-averaged capacitance and operating real porous carbon electrodes between sea and river concentrations could be problematic. To avoid such problems, it might be interesting to operate a series of blue engine capacitors with intermediate reservoirs at intermediate concentrations instead of using only one engine over the whole concentration gradient. Here, balancing the flushing and canonical steps could allow for tuning the intermediate concentrations. We have not pursued this next optimization step in detail yet.

7. Discussion and conclusions

In this article, we studied cyclic processes involving supercapacitors immersed in water at low and high salt concentration for the purpose of energy harvesting and desalination. In this context, we investigated ions within the

restricted primitive model in the micro- and mesopores of the supercapacitor electrodes at different electrostatic potentials. We compared a set of available theories, ranging from simple Poisson–Boltzmann up to sophisticated density functional theories. To distinguish between these theories and define their applicable parameter settings, we also performed molecular dynamics simulations. We found best agreement with these simulations for a fundamental measure density functional theory with mean-field Coulombic ion interactions, taking excess correlations beyond the pure Coulomb and pure hard interactions into account [30]. In agreement with earlier studies [30, 36, 45–47], we found that ion sizes cannot be neglected if a qualitative or, even more, a quantitative description of systems similar to those we studied is of interest. For mesopores, dilute ion concentrations or low potentials, simple theories like modified Poisson–Boltzmann theory [26] are still applicable. However, we show that in the micropores, where the hydrated ion size becomes of the same order of magnitude as the pore width, packing effects *do* become important and the mean field theories do not agree with simulations. For such settings, correlations between the ions must be taken into account in more elaborate theories like our density functional approach.

In the context of cyclic processes, our density functional approach predicts a significant larger amount of energy that can be harvested from blue engines than the more simple theories in our study. Relatedly, it predicts a larger consumption of energy for the desalination of water. Furthermore, we found that the (theoretical) description of the solvent has a high impact on these predictions. Here we found that taking into account the dependency of the dielectric constant on the salt concentration corrects the amount of available energy due to a concentration gradient downwards. Moreover, this treatment of the solvent predicts a potential range for the optimal operation of a blue engine around an electrode potential $\Psi \approx 0.2$ V. Consequently, a desalination device could be optimized by shifting this operational range to lower or higher potentials.

Within further research our theoretical description could be improved. While we described the solvent by a uniform dielectric constant, an explicit description of the water molecules could lead to a more accurate picture of the electric double layer [29, 37]. Moreover, for dense packings, an explicit description of the hydration shell becomes important [77, 78] to allow for the dehydration of ions near walls or in the smallest pores [25, 79] and for similar effects, where the polarizability of the water molecules plays a role. Furthermore, we described the rich geometry of the porous carbon electrode by a relatively simple parallel-plate capacitor model, neglecting effects due to the pore curvature [14] or roughness of the electrode surface [15]. In addition, carbon electrodes show metallic behaviour and accounting for image charge effects can modify the salt adsorption at low voltages [80]. Nevertheless, our findings from the parallel plate model might have interesting applications for the conversion between mechanical and electric energy [81]. Finally, dynamics can be taken into account to address the possibly slow ion transport through the pore network of the carbon electrode. This could provide the power performance of a blue engine which might highly deviate from the quasi-static calculations, which only address the energy of a cycle. However, recent simulation results show that agreement between the quasi-static calculations and dynamical studies is better than might be expected [82].

Further research could also study the implications of our findings on so-called flow electrodes [83, 84]. These devices provide an interesting alternative to the solid porous carbon electrodes used in conventional desalination devices. They consist of micron size particles of nano porous carbon in a suspension which allows to control the salt uptake by varying the feed velocity of the carbon slurry.

In a more general context, our findings also are suitable for studying the storage of energy in ionic-liquid supercapacitors. In such systems, the screening length is much shorter than in an aqueous solution. In addition, ionic liquids have a larger potential window in comparison to water. For this reason, higher potentials can be applied and ionic packing effects become even more important. Nevertheless, even very high packings of spheres are well described within fundamental measure density functional theory. Moreover, numeric calculations within this theoretical framework are much faster than computer simulations. Thus, the studied approach represents a promising starting point for more complex models or to derive from it more advanced theoretical descriptions for future research.

Acknowledgments

We thank D Brogioli and Y Levin for fruitful discussions. This work is part of the D-ITP consortium, a program of the Netherlands Organisation for Scientific Research (NWO) that is funded by the Dutch Ministry of Education, Culture and Science (OCW). We also acknowledge financial support from a NWO-VICI grant.

References

[1] Post V E, Groen J, Kooi H, Person M, Ge S and Edmunds W M 2013 *Nature* **504** 71
[2] Norman R S 1974 *Science* **186** 350
[3] Logan B E and Elimelech M 2012 *Nature* **488** 313
[4] Gerstandt K, Peinemann K V, Skilhagen S E, Thorsen T and Holt T 2008 *Desalination* **224** 64
[5] Lin S, Straub A P and Elimelech M 2014 *Energy Environ. Sci.* **7** 2706
[6] Post J W, Veerman J, Hamelers H V, Euverink G J, Metz S J, Nymeijer K and Buisman C J 2007 *J. Memb. Sci.* **288** 218
[7] Brogioli D 2009 *Phys. Rev. Lett.* **103** 058501
[8] Rica R A, Ziano R, Salerno D, Mantegazza F, van Roij R and Brogioli D 2013 *Entropy* **15** 1388
[9] Porada S, Borchardt L, Oschatz M, Bryjak M, Atchison J S, Keesman K J, Kaskel S, Biesheuvel P M and Presser V 2013 *Energy Environ. Sci.* **6** 3700
[10] Hamelers H V M, Schaetzle O, Paz-García J M, Biesheuvel P M and Buisman C J N 2013 *Environ. Sci. Technol. Lett.* **1** 31
[11] Simon P and Gogotsi Y 2008 *Nat. Mater.* **7** 845
[12] Zhu Y *et al* 2011 *Science* **332** 1537
[13] Lastoskie C, Gubbins K E and Quirke N 1993 *J. Phys. Chem.* **97** 4786

[14] Huang J, Sumpter B G and Meunier V 2008 *Chem. Eur. J.* **14** 6614
[15] Merlet C, Péan C, Rotenberg B, Madden P A, Simon P and Salanne M 2013 *J. Phys. Chem. Lett.* **4** 264
[16] Jiang D, Jin Z and Wu J 2011 *Nano Lett.* **11** 5373
[17] Kondrat S, Pérez C R, Presser V, Gogotsi Y and Kornyshev A A 2012 *Energy Environ. Sci.* **5** 6474
[18] Jiang D, Jin Z, Henderson D and Wu J 2012 *J. Phys. Chem. Lett.* **3** 1727
[19] Tran C and Kalra V 2013 *J. Power Sources* **235** 289
[20] Marino M, Misuri L, Jiménez M L, Ahualli S, Kozynchenko O, Tennison S, Bryjak M and Brogioli D 2014 *J. Colloid Interface Sci.* **436** 146
[21] Gouy M 1910 *J. Phys. Theor. Appl.* **9** 457
[22] Chapman D 1913 *Phil. Mag.* **25** 475
[23] Torrie G M and Valleau J P 1980 *J. Chem. Phys.* **73** 5807
[24] Fedorov M V and Kornyshev A A 2008 *J. Phys. Chem. Lett.* B **112** 11868
[25] Merlet C, Rotenberg B, Madden P A, Taberna P L, Simon P, Gogotsi Y and Salanne M 2012 *Nat. Mater.* **11** 306
[26] Kornyshev A A 2007 *J. Phys. Chem.* B **111** 5545
[27] Bazant M, Storey B D and Kornyshev A A 2011 *Phys. Rev. Lett.* **106** 046102
[28] Wu J 2006 *AIChE J.* **52** 1169
[29] Biben T, Hansen J P and Rosenfeld Y 1998 *Phys. Rev.* E **57** R3727
[30] Mier-y-Teran L, Suh S H, White H S and Davis H T 1990 *J. Chem. Phys.* **92** 5087
[31] Gillespie D, Nonner W and Eisenberg R S 2003 *Phys. Rev.* E **68** 031503
[32] Antypov D, Barbosa M C and Holm C 2005 *Phys. Rev.* E **71** 061106
[33] Jiang D, Meng D and Wu J 2011 *Chem. Phys. Lett.* **504** 153
[34] Forsman J, Woodward C E and Trulsson M 2011 *J. Phys. Chem.* B **115** 4606
[35] Wang Z, Liu L and Neretnieks I 2011 *J. Phys.: Condens. Matter* **23** 175002
[36] Frydel D and Levin Y 2012 *J. Chem. Phys.* **137** 164703
[37] Henderson D, Jiang D, Jin Z and Wu J 2012 *J. Phys. Chem.* B **116** 11356
[38] Evans R 1979 *Adv. Phys.* **28** 143
[39] Jeanmairet G, Levesque M, Vuilleumier R and Borgis D 2013 *J. Phys. Chem. Lett.* **4** 619
[40] Jiang D and Wu J 2013 *J. Phys. Chem. Lett.* **4** 1260
[41] Georgi N, Kornyshev A and Fedorov M 2010 *J. Electroanal. Chem.* **649** 261
[42] Han Y, Huang S and Yan T 2014 *J. Phys.: Condens. Matter* **26** 284103
[43] Breitsprecher K, Kosovan P and Holm C 2014 *J. Phys.: Condens. Matter* **26** 284108
[44] Pizio O and Sokolowski S 2014 *Condens. Matter Phys.* **17** 23603
[45] Tang Z, Mier-y-Teran L, Davis H T, Scriven L E and White H S 1990 *Mol. Phys.* **71** 369
[46] Yu Y X, Wu J Z and Gao G H 2004 *Chin. J. Chem. Eng.* **12** 688
[47] Yu Y X, Wu J Z and Gao G H 2004 *J. Chem. Phys.* **120** 7223
[48] Hansen-Goos H and Roth R 2006 *J.Phys.: Condens.Matter* **18** 8413
[49] Rosenfeld Y 1989 *Phys. Rev. Lett.* **63** 980
[50] Roth R 2010 *J. Phys.: Condens. Matter* **22** 063102
[51] Oettel M, Görig S, Härtel A, Löwen H, Radu M and Schilling T 2010 *Phys. Rev.* E **82** 051404
[52] Härtel A, Oettel M, Rozas R E, Egelhaaf S U, Horbach J and Löwen H 2012 *Phys. Rev. Lett.* **108** 226101
[53] Boon N and van Roij R 2011 *Mol. Phys.* **109** 1229
[54] van Roij R 2014 Statistical thermodynamics of supercapacitors and blue engines *Electrostatics of Soft and Disordered Matter* ed D Dean *et al* (Hoboken: Pan Stanford) chapter 19, pp 263–78
[55] Rouquerol J, Avnir D, Fairbridge C W, Everett D H, Haynes J M, Pernicone N, Ramsay J D F, Sing K S W and Unger K K 1994 *Pure Appl. Chem.* **66** 1739
[56] Janssen M, Härtel A and van Roij R 2014 *Phys. Rev. Lett.* **113** 268501
[57] Wang Z, Liu L and Neretnieks I 2011 *J. Chem. Phys.* **135** 244107
[58] Lukšic M, Hribar-Lee B, Tochimani S B and Pizio O 2012 *Mol. Phys.* **110** 17
[59] Tarazona P, Cuesta J A and Martínez-Ratón Y 2008 *Density Functional Theories of Hard Particle Systems* (*Lecture Notes in Physics* vol 753) (Berlin: Springer) chapter 7, pp 247–341
[60] Hansen J P and McDonald I R 2006 *Theory of Simple Liquids* 3rd edn (New York: Elsevier)
[61] Waisman E and Lebowitz J L 1970 *J. Chem. Phys.* **52** 4307
[62] Limbach H J, Arnold A, Mann B A and Holm C 2006 *Comput. Phys. Commun.* **174** 704
[63] Arnold A, Lenz O, Kesselheim S, Weeber R, Fahrenberger F, Roehm D, Košovan P and Holm C 2013 ESPResSo 3.1: molecular dynamics software for coarse-grained models *Meshfree Methods for Partial Differential Equations VI* (*Lecture Notes in Computational Science and Engineering* vol 89) ed M Griebel and M A Schweitzer (Berlin: Springer) pp 1–23
[64] Jover J, Haslam A J, Galindo A, Jackson G and Müller E A 2012 *J. Chem. Phys.* **137** 144505
[65] de Joannis J, Arnold A and Holm C 2002 *J. Chem. Phys.* **117** 2503
[66] Kovács R, Valiskó M and Boda D 2012 *Condens. Matter Phys.* **15** 23803
[67] Ng K C 1974 *J. Chem. Phys.* **61** 2680
[68] Oğuz E C, Messina R and Löwen H 2009 *J. Phys.: Condens. Matter* **21** 424110
[69] Deb D, Winkler A, Yamani M H, Oettel M, Virnau P and Binder K 2011 *J. Chem. Phys.* **134** 214706
[70] Oğuz E, Marechal M, Ramiro-Manzano F, Rodriguez I, Messina R, Meseguer F and Löwen H 2012 *Phys. Rev. Lett.* **109** 218301
[71] Fernández D P, Goodwin A R H, Lemmon E W, Sengers J M H L and Williams R C 1997 *J. Phys. Chem. Ref. Data* **26** 1125
[72] Sambriski E J, Schwartz D C and de Pablo J J 2009 *Biophys. J.* **96** 1675
[73] Islam M M, Alam M T and Ohsaka T 2008 *J. Phys. Chem.* C **112** 16568
[74] Cannes C, Cachet H, Debiemme-Chouvy C, Deslouis C, de Sanoit J, Le Naour C and Zinovyeva V A 2013 *J. Phys. Chem.* C **117** 22915
[75] Ahualli S, Fernández M M, Iglesias G, Delgado A V and Jiménez M L 2014 *Environ. Sci. Technol.* **48** 12378
[76] Sales B B, Burheim O S, Porada S, Presser V, Buisman C J N and Hamelers H V M 2014 *Environ. Sci. Technol. Lett.* **1** 356
[77] Levy A, Andelman D and Orland H 2012 *Phys. Rev. Lett.* **108** 227801
[78] Bankura A, Carnevale V and Klein M L 2013 *J. Chem. Phys.* **138** 014501
[79] Ohkubo T, Konishi T, Hattori Y, Kanoh H, Fujikawa T and Kaneko K 2002 *J. Am. Chem. Soc.* **124** 11860
[80] Biesheuvel P M, Porada S, Levi M and Bazant M Z 2014 *J. Solid State Electrochem.* **18** 1365
[81] Moon J K, Jeong J, Lee D and Pak H K 2013 *Nat. Commun.* **4** 1487
[82] Péan C, Merlet C, Rotenberg B, Madden P A, Taberna P L, Daffos B, Salanne M and Simon P 2014 *ACS Nano* **8** 1576
[83] Jeon S, Park H, Yeo J, Yang S C, Cho C H, Han M H and Kim D K 2013 *Energy Environ. Sci.* **6** 1471
[84] Porada S, Weingarth D, Hamelers H V M, Bryjak M, Presser V and Biesheuvel P M 2014 *J. Mater. Chem.* A **2** 9313